Optics Letters

Flexible and rapid fabrication of silver microheaters with spatial-modulated multifoci by femtosecond laser multiphoton reduction

Dongdong Qian,[1,†] Liang Yang,[1,†] Yacao Zhang,[1] Chen Xin,[1] Zhijiang Hu,[1] Kai Hu,[1] Yulong Wang,[1] Deng Pan,[1] Jiawen Li,[1,*] Dong Wu,[1,2] Yanlei Hu,[1] and Jiaru Chu[1]

[1]CAS Key Laboratory of Mechanical Behavior and Design of Materials, Department of Precision Machinery and Precision Instrumentation, University of Science and Technology of China, Hefei, Anhui 230027, China
[2]e-mail: dongwu@ustc.edu.cn
*Corresponding author: jwl@ustc.edu.cn

Received 28 August 2018; revised 24 September 2018; accepted 28 September 2018; posted 1 October 2018 (Doc. ID 344352); published 24 October 2018

In this Letter, parallel writing of silver microwire (AgMW) arrays based on femtosecond laser multiphoton reduction (MPR) is realized by modulating a femtosecond laser beam into a multifoci pattern with a spatial light modulator (SLM). Arbitrarily distributed multifoci are generated with predesigned holograms loaded on a SLM for MPR. The experimental parameters for the desired fabrication of AgMWs with multifoci are systematically investigated and optimized. On this basis, different AgMW patterns are dynamically and simultaneously fabricated by loading different holograms onto a high-frequency refreshed SLM in sequence. The quantity and distribution of multifoci can be controlled dynamically by the SLM in the fabrication process, and even the intensity of individual focus is dynamically modulated by the control of the gray level of holograms. Finally, the potential application of this flexible and rapid AgMW fabrication method in microheater fabrication is demonstrated. The microheaters exhibit a controllable temperature gradient after energized.

https://doi.org/10.1364/OL.43.005335

In recent years, metal micronanowires (MMNWs) have wide applications in many fields including photovoltaic systems [1], organic light-emitting diodes [2], electromagnetic devices [3], surface-enhanced Raman scattering substrates [4], and transparent film heaters [5–7] due to their high electrical conductivity, fine mechanical flexibility, and low manufacturing cost. So far, several methods have been developed for the fabrication of MMNWs. The most common technique is ultraviolet photolithography [8], which has been widely used in microelectromechanical systems. However, this method not only requires a customized mask, but also needs many complicated processing steps. Inkjet printing technology [9] is another technique that can fabricate MMNWs by using nozzles to spray a mixture containing metal nanoparticles (NPs). Nevertheless, the nozzles are easily clogged by metal NPs, and the diameter of the printed MMNWs is seriously limited by the diameter of the nozzles. The polyol process [10] is an alternative method that can synthesize MMNWs by reducing the corresponding metal salt in the presence of polyvinylpyrrolidone in ethylene glycol. However, the MMNWs synthesized by this method are limited in length and disorderly in distribution. Besides, none of these methods can combine flexibility, fabrication precision, and efficiency together.

Femtosecond laser direct writing has demonstrated its high spatial resolution and flexibility in three-dimensional (3D) fabrication of micro/nanostructures [11]. Femtosecond laser direct writing of MMNWs by reducing metal ions has been realized and presents high resolution as well as simple fabrication steps [12]. However, a noteworthy drawback of this technique lies in the point-by-point fabrication method, which greatly hinders its processing speed and flexibility, especially for complex microcircuits.

In this Letter, by using a spatial light modulator (SLM) to modulate a femtosecond laser beam into multifoci patterns, silver microwire (AgMW) pattern arrays are rapidly fabricated combining with the multiphoton reduction (MPR) technique. The use of the femtosecond laser multifoci fabrication technique in MPR of metal microstructures is systematically studied. The dependence of the quality of AgMWs on laser parameters, including laser power, scanning speed, and number of scans, is investigated. Moreover, different AgMW patterns are simultaneously fabricated by dynamically changing the distribution of multifoci. Not only the quantity and distribution of multifoci can be dynamically controlled, but also the scanning routes, speed, and even the intensity of each focus can be individually controlled in the fabrication process. Finally, various microheaters are rapidly and flexibly fabricated by synchronously adjusting the light intensity and scanning routes of laser foci.

The procedure of flexible direct writing of AgMWs is shown in Fig. 1(a). First, silver precursor, which is prepared by dripping a suitable amount of ammonia into a mixture of silver

nitrate solution (0.083 molL^{-1}) and trisodium citrate solution (0.062 molL^{-1}), is filled in a polydimethylsiloxane (PDMS) cavity on a glass substrate. The linear absorption coefficient of the silver precursor calculated according to the transmission fit is 1.087 cm^{-1}. Two-photon and three-photon absorbance of the silver precursor are 0.02 and 0.073, respectively [12]. Second, the silver precursor is sandwiched with a cover glass. Third, femtosecond laser (Coherent Chameleon; center wavelength, 800 nm) is tightly focused into the inner surface of the cover glass for photoreduction. Finally, the cover glass is peeled off and washed in deionized water. The temperature accumulation of the pulsed laser is calculated according to Ref. [13]. With 10 μm/s scanning speed in our experiment, the temperature accumulation of the pulsed laser is $3.56T_1$. Here, T_1 = const. is the temperature jump for one pulse. Under femtosecond laser irradiation, reduction occurs immediately due to the multiphoton absorption process [Fig. 1(b)] [12], which induces the reduction of the silver ions to silver nanoparticles (AgNPs). The MPR process can be divided into three stages [14]: nucleation, growth, and aggregation of metal NPs to form micro/nanostructure [Fig. 1(c)]. Tightly focused ultrafast laser pulses have to be employed to transfer a massive amount of photon energy (with a power density of 9.359×10^8 W/cm^2 when the laser power is 3 mW) for metal ion reduction [15]. The basic mechanism of photoreduction is a combined action of photo and thermal [14,16,17]. The resistivity of the fabricated AgMW decreases from 8.4×10^{-7} Ωm to 3.4×10^{-7} Ωm as the laser power increases from 3 mW to 5 mW. We assume that this may be due to the decrease in the particle–particle intervals on the surface of the AgMW.

In order to improve the speed and flexibility of femtosecond laser MPR, SLM is introduced into the femtosecond laser MPR system and the femtosecond laser beam is modulated into a predesigned multifoci pattern for MPR of AgMWs [Fig. 2(a)]. A computer-generated hologram (CGH) generated by Gerchberg–Saxton (GS) algorithm [18] is loaded on the SLM. The femtosecond laser beam is modulated into multifoci that distributed in a predesigned two-dimensional pattern at the focal plane of Lens 1 [Fig. 2(b)]. Since the SLM is a diffractive optical device, the modulated femtosecond laser beam will produce multiple diffraction orders. To filter the first order,

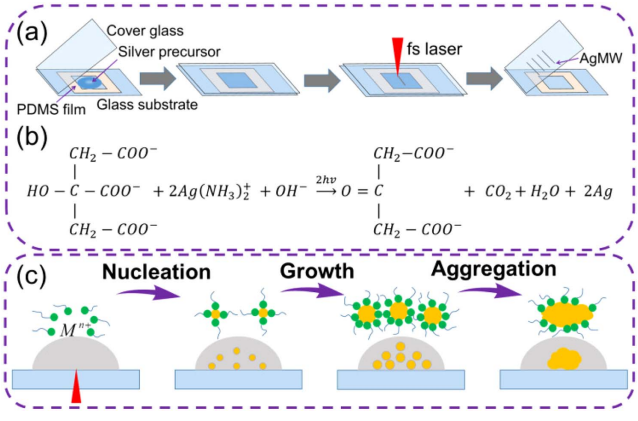

Fig. 1. Fabrication of AgMWs by femtosecond laser-induced MPR. (a) Schematic illustration of the process of the fabrication of AgMWs on cover glass by femtosecond laser-induced MPR. (b) The reaction equation of the multiphoton absorption process. (c) Schematic process of silver pattern forming: nucleation; growth; and then, aggregation.

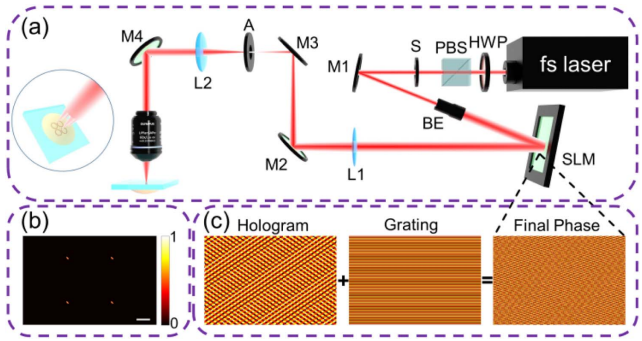

Fig. 2. Creation of the multifoci pattern for femtosecond laser multifoci MPR of the AgMW pattern array. (a) Experimental setup: HWP, half-wave plate; PBS, polarizing beam splitter; S, shutter; M, mirror; BE, beam expander; SLM, spatial light modulator; L, lens; A, aperture. Inset, schematic diagram of multifoci fabrication of the AgMW circle array in the silver precursor sample. (b) Calculated intensity distribution of multiple focuses at the focus plane of Lens 1. The scale bar is 10 μm. (c) The superposition of blazed grating and CGH to separate the multifoci beam from the zero-diffraction order.

which is desired, from other unwanted diffraction orders, a blazed grating phase pattern is superposed to the CGH [Fig. 2(c)]. The multifoci beam array is then focused into the silver precursor sample fixed on a 3D precision piezo stage with an oil-immersion objective lens after passing through Lens 2. By controlling the movement of the piezo stage with a computer, multifoci fabricating of the AgMW pattern array can be achieved.

For high-precision fabrication of AgMWs with a multifoci pattern, the experimental parameters need to be optimized. The dependence of the width and height of the AgMWs on the laser power, scanning speed, and number of scans are systematically investigated. Figures 3(a) and 3(b) show the scanning electron microscope (SEM) image and atomic force microscope (AFM) image of AgMWs fabricated with laser power varying from 0.8 mW to 6 mW while the scanning speed and number of scans are kept at 10 μm/s and 1 time, respectively. The width/height of the AgMWs increase from 0.814 μm/31 nm to 1.995 μm/60 nm when the laser power changes from 0.8 mW to 6 mW [Fig. 3(c)]. It is found that there is a threshold power for reduction, and when the laser power is lower than 0.8 mW, AgMWs become discontinuous. Moreover, the scanning speed also plays an important role in determining the width and height of the AgMWs. Figures 3(d) and 3(e) show the SEM image and AFM image of AgMWs fabricated with the scanning speed varying from 1 μm/s to 30 μm/s while the laser power and number of scans are kept at 3 mW and 1 time, respectively. Both the width and height of the AgMWs decrease with the increasing of the scanning speed [Fig. 3(f)]. The AgMWs become intermittent when the scanning speed exceeds 30 μm/s. It is reasonable that there are not enough AgNPs to aggregate into a continuous nanowire owing to the decreased amount of the reduced AgNPs when the scanning speed exceeds 30 μm/s. In addition, the effect of the number of scans on the width and height of the AgMWs is investigated. Figures 3(g) and 3(h) show the SEM image and AFM image of AgMWs fabricated with a different number of scans while the laser power and scanning speed are kept at 3 mW and 10 μm/s, respectively. As the number of scans

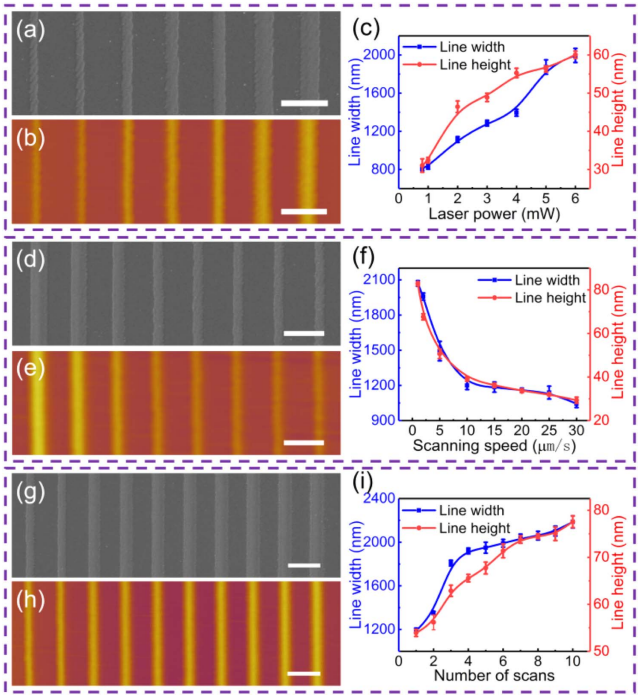

Fig. 3. SEM and AFM images of AgMWs fabricated under different laser processing parameters, and the corresponding width and height dependence on the laser power, scanning speed, and number of scans. (a) AgMWs fabricated while varying the laser power from 0.8 mW to 6 mW. (d) AgMWs fabricated while varying the scanning speed from 1 μm/s to 30 μm/s. (g) AgMWs fabricated while varying the number of scans from 1 time to 10 times. (b), (e), and (h) are AFM images of AgMWs corresponding to (a), (d), and (g), respectively. (c), (f), and (i) are the dependence of width and height of the AgMWs on the laser power, scanning speed, and number of scans, respectively. The scale bars are 5 μm.

increases, the width and height of the AgMWs increase correspondingly, as shown in Fig. 3(i).

Compared with single-focus MPR technology, multifoci MPR technology not only has better fabrication flexibility, but also greatly improves the fabrication speed. As shown in Figs. 4(a) and 4(b), four foci are generated at one time and the pentagonal array, spiral array (see Visualization 1), and Olympic logo array are obtained by scanning the four foci simultaneously [Figs. 4(e)–4(g)]. Due to the scanning speed of the femtosecond laser used in the experiment being 2 μm/s, the fabricating time of these arrays is 25 s, 36.4 s, and 125.6 s, respectively, which is one quarter of that by single-focus MPR. Moreover, any two-dimensional AgMW pattern array can be rapidly fabricated by designing the scanning routes of multifoci.

The most remarkable advantage of femtosecond laser multifoci MPR technology is that the number and distribution of multiple foci can be dynamically adjusted by loading the CGHs, which gives this technology great flexibility. As shown in Figs. 4(h)–4(j), different numbers and distributions of pentagram arrays have been fabricated by loading three-, four-, and seven-foci CGHs onto the SLM. The distances between multiple foci are controlled to be 38.7 μm and 27.8 μm for the three-foci pattern [Fig. 4(h)], 41.7 μm and 27.8 μm for the four-foci pattern [Fig. 4(i)], and 46.4 μm and 33.3 μm for the seven-foci pattern [Fig. 4(j)].

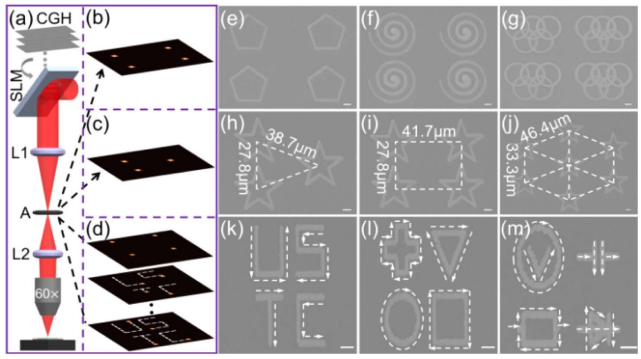

Fig. 4. Complex AgMW patterns fabricated by femtosecond laser multifoci MPR. (a) Schematic illustration of multifoci modulation. Calculated intensity distribution of the (b) four foci and (c) three foci corresponds to (e) and (h), respectively. (d) Calculated intensity distribution of the four dynamic foci and their scanning routes indicated by white dotted lines corresponds to (k). (e)–(g) SEM images of the pentagonal array, spiral array, and Olympic logo array, respectively. SEM images of the pentagram arrays distributed in (h) isosceles triangle, (i) rectangle, and (j) hexagon pattern. (k) SEM image of a "USTC" pattern formed by dynamically scanning the four foci along individual routes. White dotted lines with arrows indicate the scanning routes of different focuses. (l) and (m) are SEM images of various patterns formed by a similar fabrication method to (k). The scale bars are 5 μm.

In addition to flexible modulation of the quantity and distribution of multiple foci, the location of the multiple foci can be dynamically modulated when fabricating AgMWs by sequentially loading predesigned CGHs. This method eliminated the requirement of precise equipment to control the scanning routes of foci, which means the motion control part of the fabrication system can be greatly simplified. As shown in Figs. 4(a) and 4(d), when loading series-predesigned CGHs onto the SLM in sequence, the four foci are dynamically modulated to move along the "U," "S," "T," and "C" routes individually and simultaneously in the focal plane of objective (see Visualization 2). Thus, a "USTC" AgMW pattern [Fig. 4(k)] is fabricated without the need of any movement of mechanical or optical devices. The fabricating time of the entire pattern only takes 10 s. Besides, any other two-dimensional pattern can be fabricated by using this novel femtosecond laser multifoci MPR technology. For example, some geometry patterns have been fabricated, such as the cross, triangle, circle, and square shown in Fig. 4(l) as well as symbols of electronic components, such as the voltmeter, capacitor, resistor, and diode shown in Fig. 4(m).

To demonstrate the potential application of this flexible and rapid AgMW fabrication method in microheater application, microheaters [Fig. 5] are fabricated with femtosecond laser multifoci MPR between two electrodes on the cover glass and finally passivated by deposition of a 100-nm-thick SiO_2 layer. By controlling the gray values of CGHs, the light intensity of the two foci can be controlled individually. The two foci with the same light intensity are used to fabricate the labyrinth and spiral microheater in Figs. 5(a) and 5(i), while two foci with different light intensity are adopted for the microheaters fabrication in Figs. 5(e) and 5(m). The linewidths in Figs. 5(a) and 5(i) are uniform, while the linewidths in Figs. 5(e) and 5(m) are different for the left and right coils.

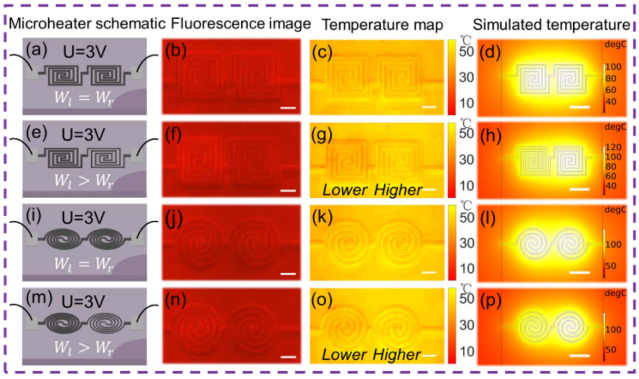

Fig. 5. Heating capacity verification and temperature field measurement and simulation of four microheaters fabricated by multifoci MPR technology. The first column is the schematic diagram of the four microheaters. W_l and W_r represent the AgMW width of the left and right coils, respectively. The second column shows the rhodamine B fluorescence images after the four microheaters being applied with a voltage of 3 V for 30 s. The third column shows the temperature profile of the four microheaters after the conversion of the relative fluorescence intensity to temperature field. The fourth column shows the simulated temperature profile. The scale bars are 10 μm in (b), (c), (f), (g), (j), (k), (n), and (o), and 20 μm in (d), (h), (l), and (p).

After spreading a dense layer of rhodamine B molecules on the microheater surfaces, a voltage of 3 V is applied to the nickel electrodes. It can be clearly seen that the fluorescence intensity of rhodamine B gradually weakens after the microheaters are energized. In fact, the higher the temperature is on a certain area of the microheater surface, the weaker the fluorescence intensity of rhodamine B will be in the area. This also confirms the heating capability of the microheaters. The second column of Fig. 5 shows the fluorescence images of rhodamine B after 30 s energization of the microheaters. According to the calibration curve, the relative fluorescence intensity of rhodamine B is converted to temperature values and is expressed as temperature distribution images in the third column of Fig. 5. Since the coils on two sides of the microheaters have the same resistance, the temperature distribution is almost the same [Figs. 5(c) and 5(k)]. When the resistances of the coils on two sides are different, the temperature distribution is different [Figs. 5(g) and 5(o)].

In order to gain further insight into the temperature distribution on the surface of the microheaters, COMSOL is used to simulate the surface temperature of the microheaters. The simulation results are shown in the fourth column of Fig. 5, which are consistent with the measured temperature field. For example, the temperature distribution of the left and right coils of the microheater is the same, and the maximum temperature is about 105°C [Fig. 5(d)]. In contrast, the temperature distribution of the right coil of the microheater is higher than that of the left coil, and the maximum temperature of the right coil is about 120°C, while the left coil is about 100°C of the left coil [Fig. 5(h)]. However, the measured surface temperatures are lower than that of the simulation. This is because the measured temperature values may be lower than the actual temperature due to the photobleaching effect of rhodamine B when exposed to light for observation [19].

In conclusion, femtosecond laser multifoci direct writing is combined with MPR technology for rapid and flexible fabrication of AgMWs. By loading predesigned CGHs onto SLM, a femtosecond laser beam is modulated into an arbitrary desired multifoci pattern. The quantity and distribution of multifoci are dynamically controlled by SLM in the fabrication process. The scanning routes, speed, and even the intensity of each focus can be individually controlled. The experimental parameters for high-precision fabrication of AgMWs with multifoci are optimized. Finally, various microheaters with finer heating capability are fabricated, and their surface temperature profiles are experimentally measured, which are consistent with theoretical simulation. This highly dynamic multifoci MPR method has superior advantage in the fabrication of microheaters with a complex pattern and controllable temperature gradient and further exhibits prospective application in fields including surface-enhanced Raman scattering substrates, flexible electronics, microfluidic devices, and metamaterials.

Funding. National Key Research and Development Program of China (2018YFB1105400); National Natural Science Foundation of China (NSFC) (51675503, 51805508, 51805509, 51875544, 61475149, 61805230); Fundamental Research Funds for the Central Universities (WK 2090090012, WK2480000002, WK2090090021); Youth Innovation Promotion Association of the Chinese Academy of Sciences (2017495).

Acknowledgment. This work was partially carried out at the USTC Center for Micro and Nanoscale Research and Fabrication.

†These authors contributed equally to this work.

REFERENCES

1. J. H. Yim, S. Y. Joe, C. Pang, K. M. Lee, H. Jeong, J. Y. Park, Y. H. Ahn, J. C. de Mello, and S. Lee, ACS Nano **8**, 2857 (2014).
2. H. G. Im, S. H. Jung, J. Jin, D. Lee, J. Lee, D. Lee, J. Y. Lee, I. D. Kim, and B. S. Bae, ACS Nano **8**, 10973 (2014).
3. C. Yang, H. Gu, W. Lin, M. M. Yuen, C. P. Wong, M. Xiong, and B. Gao, Adv. Mater. **23**, 3052 (2011).
4. I. Izquierdo-Lorenzo, S. Jradi, and P. M. Adam, RSC Adv. **4**, 4128 (2014).
5. S. Hong, H. Lee, J. Lee, J. Kwon, S. Han, Y. D. Suh, H. Cho, J. Shin, J. Yeo, and S. H. Ko, Adv. Mater. **27**, 4744 (2015).
6. S. Ji, W. He, K. Wang, Y. Ran, and C. Ye, Small **10**, 4951 (2014).
7. T. Kim, Y. W. Kim, H. S. Lee, H. Kim, W. S. Yang, and K. S. Suh, Adv. Funct. Mater. **23**, 1250 (2013).
8. R. F. Pease and S. Y. Chou, Proc. IEEE **96**, 248 (2008).
9. J. Jiang, B. Bao, M. Li, J. Sun, C. Zhang, Y. Li, F. Li, X. Yao, and Y. Song, Adv. Mater. **28**, 1420 (2016).
10. Y. Sun and Y. Xia, Adv. Mater. **14**, 833 (2002).
11. Y. Zhang, Q. Chen, H. Xia, and H. Sun, Nano Today **5**(5), 435 (2010).
12. B. Xu, H. Xia, L. Niu, Y. Zhang, K. Sun, Q. Chen, Y. Xu, Z. Lv, Z. Li, H. Misawa, and H. Sun, Small **6**, 1762 (2010).
13. S. Rekstyte, T. Jonavicius, D. Gailevicius, M. Malinauskas, V. Mizeikis, E. G. Gamaly, and S. Juodkazis, Adv. Opt. Mater. **4**, 1209 (2016).
14. Y. Cao, N. Takeyasu, T. Tanaka, X. Duan, and S. Kawata, Small **5**, 1144 (2009).
15. K. Miura, J. R. Qiu, T. Mitsuyu, and K. Hirao, Proc. SPIE **3618**, 141 (1999).
16. S. Tabrizi, Y. Cao, B. P. Cumming, B. Jia, and M. Gu, Adv. Opt. Mater. **4**, 529 (2016).
17. L. D. Zarzar, B. S. Swartzentruber, B. F. Donovan, P. E. Hopkins, and B. Kaehr, ACS Appl. Mater. Interfaces **8**, 21134 (2016).
18. R. W. Gerchberg and W. O. Saxton, Optik **35**, 237 (1972).
19. P. Low, B. Kim, N. Takama, and C. Bergaud, Small **4**, 908 (2008).